A Computational Model for Tracking Subsurface Tissue Deformation During Stereotactic Neurosurgery

Keith D. Paulsen,* *Member, IEEE*, Michael I. Miga, Francis E. Kennedy, P. Jack Hoopes, Alex Hartov, and David W. Roberts

***Abstract*— Recent advances in the field of sterotactic neurosurgery have made it possible to coregister preoperative computed tomography (CT) and magnetic resonance (MR) images with instrument locations in the operating field. However, accounting for intraoperative movement of brain tissue remains a challenging problem. While intraoperative CT and MR scanners record concurrent tissue motion, there is motivation to develop methodologies which would be significantly lower in cost and more widely available. The approach we present is a computational model of brain tissue deformation that could be used in conjunction with a limited amount of concurrently obtained operative data to estimate subsurface tissue motion. Specifically, we report on the initial development of a finite element model of brain tissue adapted from consolidation theory. Validations of the computational mathematics in two and three dimensions are shown with errors of 1%–2% for the discretizations used. Experience with the computational strategy for estimating surgically induced brain tissue motion *in vivo* is also presented. While the predicted tissue displacements differ from measured values by about 15%, they suggest that exploiting a physics-based computational framework for updating preoperative imaging databases during the course of surgery has considerable merit. However, additional model and computational developments are needed before this approach can become a clinical reality.**

***Index Terms*—Brain tissue model, finite element, porous media, stereotactic neurosurgery, subsurface brain deformation.**

I. Introduction

THE technological developments of computed tomography (CT) and magnetic resonance (MR) scanning, along with the advent of low-cost high-performance computing, have radically changed the application of stereotactic principles in neurosurgery over the last twenty years. For example, the routine availability of preoperative imaging studies (initially from CT and now from MR) has enabled the diagnosis of small structural abnormalities within the brain, such as tumors, that previously would have either been diagnosed later (when larger) or in many instances remained unrecognized altogether. This has heightened the need to biopsy these lesions, many of which cannot be safely approached by other than stereotactic techniques. The availability of low-cost, high-performance computing has also significantly impacted the rise in stereotactic procedures by allowing inexpensive computer workstations to be located within the operating room (OR); this has made possible graphical displays of anatomical images integrated with spatial coordinate systems. Through computational methods which coregister spatial relationships between surgical instrument location and preoperative images, the exciting reality of accomplishing stereotactic tasks without the need for the stereotactic frame is possible [1]–[5]

The value of such computer-assisted, interactive navigational guidance during surgery has become widely appreciated as neurosurgical capability has been expanded by a methodology that is safer, more effective and more efficient [6], [7]. Concurrent with enthusiasm for this development has been a recognition of certain limitations. One of the most challenging problems has been that of misregistration of OR and image spaces arising from movement or deformation of the brain subsequent to the preoperative imaging studies upon which all stereotactic information has been based [1], [8], [9]. Upon opening of the dura and drainage of cerebrospinal fluid (CSF), tissue retraction, or partial resection, there is shifting of brain structures which invalidates the navigational reference frame derived from preoperative images. The most common approach to this problem at the present time has been to obtain updated image information in the OR using either a CT/MR scanner or intraoperative ultrasound [10]–[13]. In the former case, only a few medical centers have been able to afford the significant expense of a dedicated CT/MR scanner in the OR; in the latter case an incomplete database is provided for navigational purposes due to the significantly lower contrast resolution (i.e., only a few anatomical landmarks are visible in an ultrasound image and their visibility tends to degrade as the surgical procedure progresses) and the absence of comparable preoperative information (since ultrasound cannot generally be used through the intact cranium). As a result, in terms

Manuscript received March 10, 1997; revised June 12, 1998. This work was supported by National Institutes of Health (NIH) under Grant R01-NS33900 awarded by the National Institute of Neurological Disorders and Stroke. *Asterisk indicates corresponding author.*

*K. D. Paulsen is with the Thayer School of Engineering, Dartmouth College, Hanover, NH 03755 USA. He is also with Dartmouth Hitchcock Medical Center, Lebanon, NH 03766 USA, and Norris Cotton Cancer Center, Lebanon, NH 03766 USA (e-mail: keith.paulsen@dartmouth.edu).

M. I. Miga and F. E. Kennedy are with the Thayer School of Engineering, Dartmouth College, Hanover, NH 03755 USA.

P. J. Hoopes is with the Thayer School of Engineering, Dartmouth College, Hanover, NH 03755 USA. He is also with Dartmouth Hitchcock Medical Center, Lebanon, NH 03766 USA, and Norris Cotton Cancer Center, Lebanon, NH 03766 USA.

A. Hartov is with the Thayer School of Engineering, Dartmouth College, Hanover, NH 03755 USA. He is also with the Dartmouth Hitchcock Medical Center, Lebanon, NH 03766 USA.

D. W. Roberts is with the Dartmouth Hitchcock Medical Center, Lebanon, NH 03766 USA. He is also with the Norris Cotton Cancer Center, Lebanon, NH 03766 USA.

Publisher Item Identifier S 0018-9294(99)00830-7.

of offering a low cost solution which would be accessible to most neurosurgeons, intraoperative ultrasound does not appear, in and of itself, to be able to overcome the distortion related limitations inherent in frameless stereotaxy when based on preoperative data. Hence, there is significant motivation for and interest in the development of methodologies which would be significantly lower in cost and more widely available than dedicated intraoperative CT or MR scanners, and yet provide more complete updated anatomical information than is presently possible with intraoperative ultrasound.

Our approach to this problem is to develop a computational model of brain tissue deformation that could be used in conjunction with a limited amount of concurrently obtained operative data (e.g., video-tracked surface movement and subsurface ultrasound) to estimate subsurface tissue motion and thereby provide updated anatomical information for improved navigational assistance during frameless stereotaxy procedures. In this paper, we report on the initial development of a finite element model of brain tissue deformation intended to serve this purpose. Specifically, we have implemented a porous-media description of brain tissue taken from the soil mechanics literature [14] in two-dimensional (2-D) and three-dimensional (3-D) finite element models [15]. We have also qualitatively demonstrated the ability to incorporate several different types of surgical effects within the model including the administration of mannitol, and the drainage of CSF [15]. Here, we show validations of the computational mathematics by first solving a number of idealized benchmark problems with known solutions. We also report on our initial experience using this computational strategy for estimating surgically induced brain tissue motion in a pig brain model. The results suggest that the idea of utilizing a physics-based computational framework for updating preoperative imaging databases during the course of surgery has considerable merit, although additional model and computational developments need to occur before such an approach can become a clinical reality.

II. The Computational Model

Interestingly, there has been only a modest amount of finite element modeling of brain tissue; this can, in general, be categorized according to the type of loading conditions that have been applied. The majority of work that has been reported was performed in the 1970's and centered on head injury models where the effects of impact blows to the intact head have been studied in the context of automobile crashes [16]–[18]. In these simulations, loading conditions involving large accelerations of the cranium followed by sharp deceleration or impact have been the norm. One of the more recent studies in this vein which provides some sense of the level of model complexity achieved to date consisted of a 2-D axisymmetric plane strain computation incorporating a modest number of elements, an idealized skull and a simplified (layered) structure of cranial contents [19]. While this form of brain tissue modeling has remained somewhat idealized, it has provided the impetus to measure the mechanical properties of various brain tissue constituents which can be used in more complex models of brain deformation [20]–[23].

A second line of inquiry has recently emerged in brain tissue modeling where loading conditions associated with pathophysiologies of the brain such as hydrocephalus and hemorrhage have been investigated [24]–[29]. In this work, more sophisticated and realistic representations of the brain as a multi-phasic porous medium have been considered. At the present time, the state-of-the-art has been 2-D finite element computation where anatomical structure derived from CT data has been preserved. Current models have provided centimeter-scale discretizations of the major anatomical landmarks in axial cross-sections of the brain. While pioneering in nature, these simulations have not progressed to higher resolution or three dimensionality, nor have they considered loading conditions relevant to surgical procedures.

Our starting point for exploiting computational modeling in computer-assisted stereotactic surgery is multi-phase consolidation theory [14] which considers the brain as a sponge-like material where tissue motion is characterized by an instantaneous deformation at the area of contact followed by additional deformation resulting from exiting pore fluid driven by a pressure gradient. Others have recognized the utility of applying consolidation theory to soft tissue mechanics, including Taylor [30], [31] who created an interstitial transport model taking into account plasma protein movement and interstitial swelling. Basser [32] has also used a consolidation approach to model infusion-induced swelling in the brain. Computationally, the work of Nagashima *et al.* highlighted above represents the first and most extensive experience with consolidation in the neuroanatomy context [24]–[26].

The governing equations we have considered for consolidation in soft-tissue can be written as

$$\nabla \cdot G\nabla \boldsymbol{u} + \nabla \frac{G}{1-2\nu}(\nabla \cdot \boldsymbol{u}) - \alpha \nabla p = 0 \tag{1a}$$

$$\alpha \frac{\partial}{\partial t}(\nabla \cdot \boldsymbol{u}) + \frac{1}{S}\frac{\partial p}{\partial t} - \nabla \cdot k\nabla p = 0 \tag{1b}$$

where

- G shear modulus (Pa);
- ν Poisson's ratio;
- $\boldsymbol{u}$ displacement vector (m);
- p pore fluid pressure (Pa);
- α ratio of fluid volume extracted to volume change of the tissue under compression;
- k hydraulic conductivity $(m^3 s/kg)$;
- $1\backslash S$ amount of fluid which can be forced into the tissue under constant volume $(1/Pa)$.

These equations assume that the solid tissue behaves in a linearly elastic fashion and that the pore fluid is incompressible. Equation (1a) relates mechanical equilibrium to the fluid pressure gradient across the medium, while (1b) provides the constitutive relationship between volumetric strain and fluid pressure. Generally, the brain can be considered as a saturated medium which eliminates the time rate of change in pressure from (1b) (i.e., $\alpha = 1, 1\backslash S = 0$), and we have made this assumption in the results reported herein. Although more complex theories exist which may be applicable to brain tissue [33]–[36], consolidation physics as represented by (1) is more useful than simple linear, single phase elasticity due to

the added fluid/pressure component; it allows access to more realistic boundary conditions related to intracranial pressures and CSF drainage while maintaining linearity which is a significant computational advantage. Hence, linear consolidation theory offers a versatile but computationally practical approach to modeling tissue motion and it is in this vein we explore its utility in the context of stereotactic neurosurgery.

III. Finite Element Implementation

Galerkin weighted residual discretization begins with volume integration of (1) when multiplied by a suitable spatially continuous weighting function ϕ_i

$$\langle \phi_i \nabla \cdot G \nabla \boldsymbol{u} \rangle + \left\langle \phi_i \nabla \frac{G}{1-2\nu} (\nabla \cdot \boldsymbol{u}) \right\rangle - \langle \phi_i \nabla p \rangle = 0 \quad (2a)$$

$$\left\langle \phi_i \frac{\partial}{\partial t} (\nabla \cdot \boldsymbol{u}) \right\rangle - \langle \phi_i \nabla \cdot k \nabla p \rangle = 0 \quad (2b)$$

where $\langle \cdot \rangle$ indicates integration over the problem domain. Here, ϕ_i is the ith member of a complete set of scalar functions of position, in particular, the standard C^o local Lagrange polynomial interpolants associated with finite elements. Applying the divergence and gradient integral identities

$$\begin{aligned} \langle \nabla \cdot (G \nabla \boldsymbol{u} \phi_i) \rangle &= \oint G \hat{n} \cdot \nabla \boldsymbol{u} \phi_i \, ds \\ &= \langle \phi_i \nabla \cdot G \nabla \boldsymbol{u} \rangle + \langle G \nabla \boldsymbol{u} \cdot \nabla \phi_i \rangle \quad (3a) \\ \langle \nabla \cdot (k \nabla p \phi_i) \rangle &= \oint k \hat{n} \cdot \nabla p \phi_i \, ds \\ &= \langle \phi_i \nabla \cdot k \nabla p \rangle + \langle k \nabla p \cdot \nabla \phi_i \rangle \quad (3b) \\ \left\langle \nabla \left(\frac{G}{1-2\nu} \nabla \cdot \boldsymbol{u} \phi_i \right) \right\rangle &= \oint \frac{G}{1-2\nu} \hat{n} (\nabla \cdot \boldsymbol{u}) \phi_i \, ds \\ &= \left\langle \phi_i \nabla \left(\frac{G}{1-2\nu} \nabla \cdot \boldsymbol{u} \right) \right\rangle \\ &\quad + \left\langle \frac{G}{1-2\nu} (\nabla \cdot \boldsymbol{u}) \nabla \phi_i \right\rangle \quad (3c) \end{aligned}$$

to the second derivative terms in (2), leads to

$$\begin{aligned} &\langle G \nabla \boldsymbol{u} \cdot \nabla \phi_i \rangle + \left\langle \frac{G}{1-2\nu} (\nabla \cdot \boldsymbol{u}) \nabla \phi_i \right\rangle + \langle \phi_i \nabla p \rangle \\ &\quad = \oint G \hat{n} \cdot \nabla \boldsymbol{u} \phi_i \, ds + \oint \frac{G}{1-2\nu} \hat{n} (\nabla \cdot \boldsymbol{u}) \phi_i \, ds \quad (4a) \\ &\left\langle \phi_i \frac{\partial}{\partial t} (\nabla \cdot \boldsymbol{u}) \right\rangle + \langle k \nabla p \cdot \nabla \phi_i \rangle = \oint k \hat{n} \cdot \nabla p \phi_i \, ds \quad (4b) \end{aligned}$$

where $\oint$ denotes integration over the enclosing boundary and $\hat{n}$ is the outward-pointing normal direction to this boundary. Spatial discretization of (4) is completed in Galerkin fashion by expanding the unknown displacement vector, $\boldsymbol{u}$, and fluid pressure, p, as sums of time-varying unknown coefficients multiplied by known functions of position

$$\boldsymbol{u}(\boldsymbol{x}, t) = \sum_j \boldsymbol{u}_j(t) \phi_j(\boldsymbol{x}) \quad (5a)$$

$$p(\boldsymbol{x}, t) = \sum_j p_j(t) \phi_j(\boldsymbol{x}). \quad (5b)$$

This produces the coupled set of ordinary differential equations

$$\begin{aligned} &\sum_j \boldsymbol{u}_j \langle G \nabla \phi_j \cdot \nabla \phi_i \rangle + \sum_j \boldsymbol{u}_j \cdot \left\langle \nabla \phi_j \frac{G}{1-2\nu} \nabla \phi_i \right\rangle \\ &\qquad + \sum_j p_j \langle \nabla \phi_j \phi_i \rangle = \oint G \hat{n} \cdot \nabla \boldsymbol{u} \phi_i \, ds \\ &\qquad + \oint \frac{G}{1-2\nu} \hat{n} (\nabla \cdot \boldsymbol{u}) \phi_i \, ds \quad (6a) \\ &\sum_j \frac{\partial \boldsymbol{u}_j}{\partial t} \langle \nabla \phi_j \phi_i \rangle + \sum_j p_j \langle k \nabla \phi_j \cdot \nabla \phi_i \rangle = \oint k \hat{n} \cdot \nabla p \phi_i \, ds. \end{aligned}$$

(6b)

Equations (6) are integrated in time using the simple two-point weighting

$$\int_{t_n}^{t_{n+1}} f(t) \, dt = \Delta t [\theta f(t_{n+1}) + (1-\theta) f(t_n)]$$

where $\Delta t = t_{n+1} - t_n$ and $0 \le \theta \le 1$. In Cartesian coordinates this produces the two-time-level discrete system which is expressible as matrix equation

$$AU^{n+1} = BU^n + C^{n+\theta} \quad (7a)$$

where A is composed of the submatrices defined in (7b), shown at the bottom of the page, $\delta_k = (\partial \phi_j / \partial k) \phi_i$, $\delta_{kl} = (\partial \phi_j / \partial k)(\partial \phi_i / \partial l)$, where k and l take on the values x, y, or z and U and C are the subvectors

$$U_j^n = \begin{Bmatrix} u_{x_j}(t_n) \\ u_{y_j}(t_n) \\ u_{z_j}(t_n) \\ p_j(t_n) \end{Bmatrix} \quad (7c)$$

$$C_i^{n+\theta} = \begin{Bmatrix} \hat{x} \cdot \oint \sigma_s(t_{n+\theta}) \cdot \hat{n} \phi_i \, ds \\ \hat{y} \cdot \oint \sigma_s(t_{n+\theta}) \cdot \hat{n} \phi_i \, ds \\ \hat{z} \cdot \oint \sigma_s(t_{n+\theta}) \cdot \hat{n} \phi_i \, ds \\ \Delta t \oint k \nabla p(t_{n+\theta}) \cdot \hat{n} \phi_i \, ds \end{Bmatrix}. \quad (7d)$$

$$A_{ij} = \begin{bmatrix} \theta G \left\langle \frac{2(1-\nu)}{1-2\nu} \delta_{xx} + \delta_{yy} + \delta_{zz} \right\rangle & \theta G \left\langle \frac{2\nu}{1-2\nu} \delta_{yx} + \delta_{xy} \right\rangle & \theta G \left\langle \frac{2\nu}{1-2\nu} \delta_{zx} + \delta_{xz} \right\rangle & \theta \langle \delta_x \rangle \\ \theta G \left\langle \frac{2\nu}{1-2\nu} \delta_{xy} + \delta_{yx} \right\rangle & \theta G \left\langle \frac{2(1-\nu)}{1-2\nu} \delta_{yy} + \delta_{xx} + \delta_{zz} \right\rangle & \theta G \left\langle \frac{2\nu}{1-2\nu} \delta_{zy} + \delta_{yz} \right\rangle & \theta \langle \delta_y \rangle \\ \theta G \left\langle \frac{2\nu}{1-2\nu} \delta_{xz} + \delta_{zx} \right\rangle & \theta G \left\langle \frac{2\nu}{1-2\nu} \delta_{yz} + \delta_{zy} \right\rangle & \theta G \left\langle \frac{2(1-\nu)}{1-2\nu} \delta_{zz} + \delta_{xx} + \delta_{yy} \right\rangle & \theta \langle \delta_z \rangle \\ \langle \delta_x \rangle & \langle \delta_y \rangle & \langle \delta_z \rangle & \theta \Delta t k \langle \delta_{xx} + \delta_{yy} + \delta_{zz} \rangle \end{bmatrix} \quad (7b)$$

B is the same as A with $\tilde{\theta}$ replacing θ, where $\tilde{\theta} = \theta - 1$. In (7d) $\sigma_s(t_{n+\theta})$ is the linearly elastic stress tensor evaluated at time $t_{n+\theta}$ (i.e., $\sigma_s(t_{n+\theta}) = \theta\sigma_s(t_{n+1}) + (1-\theta)\sigma_s(t_n)$) which expresses the boundary integrals in terms of normal stresses which are the natural boundary conditions for the mechanical equilibrium equations. Note that reaching the discrete form represented by equations (7b)–(7d) requires some further manipulation of the boundary and volume terms emerging directly from the discrete version of (6) as described in the Appendix.

IV. Benchmark Test Cases

In this section, we examine the computational integrity of our FE implementation on a series of benchmark problems with known solutions. Specifically, we compute two and 3-D numerical solutions for the classical one-dimensional (1-D) consolidation column [14], 2-D numerical solutions for the 2-D strip loading problem taken from the literature [37], [38] and 3-D solutions to spherical consolidation under pressure loadings as reported by Basser [32].

The predominant analytical consolidation benchmark used for computational validation considers the compression of a column of a porous medium (typically soil, but in our application tissue) under a uniform load. The nature of the solution is 1-D but the problem can be solved numerically on two and 3-D meshes. It is illustrated in Fig. 1. The problem specifications for the domain described in Fig. 1 are

Material properties	$G = 1.0 \times 10^7\ Pa, \nu = 0.3$, $k = 1.0 \times 10^{-13}\ m^3 s/kg$;
Running properties	$dt = 1.0 \times 10^3\ s, \theta = 1$, # steps $= 1.0 \times 10^3$;
2-D mesh properties	linear triangles (319 nodes, 560 elements);
3-D mesh properties	linear tetrahedral (3509 nodes, 16 800 elements);
Boundary 1	$u_n = 0, \sigma_t = 0, (\partial p/\partial n) = 0$;
Boundary 2	$\sigma_t = 0, u_n = 0, (\partial p/\partial n) = 0$;
Boundary 3	$\sigma_t = 0, \sigma_n = p_o, p = 0$;
Initial conditions	at $t = 0, \boldsymbol{u} = 0$, and $p = p_o$.

where σ_t and σ_n are the shear and normal stresses, respectively and u_n is the normal displacement at the boundary surface.

The analytic solution to this problem for a saturated media is given by Biot [14]. Fig. 2 shows a comparison of the normalized pressure distribution and surface deformation as a function of time for the 2-D numerical computation relative to its analytical counterpart, whereas Fig. 3 presents the same comparison using the 3-D calculated results. As can be seen, the numerical results are in excellent agreement with the analytical benchmark. To quantify, the error in the 2-D computations is 1.25% of applied load and 2.25% of the maximum deformation for pressure and displacement respectively, while in 3-D, the corresponding errors are 1.4% and 1.5%, respectively.

The second benchmark we have considered is the 2-D axisymmetric striploading problem shown in Fig. 4 which has been calculated and solved analytically in the literature [38]. The mesh dimensions which must remain finite were

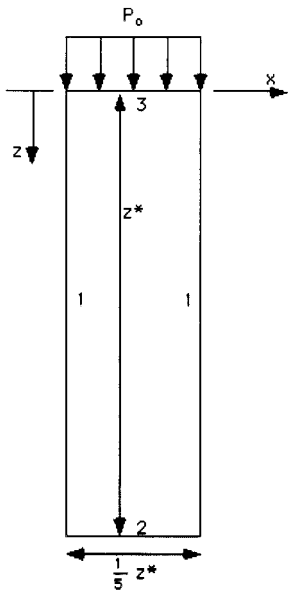

Fig. 1. One-dimensional analytical consolidation problem ($z^* = 1$ m).

constructed to minimize their effect in the solution zone according to [37] and the parameter k^* is the coefficient of permeability which is related to our hydraulic conductivity by $k = k^*/\gamma$ where γ is the specific weight of the pore fluid. The problem specifications for the domain described in Fig. 4 are as follows.

Material properties	$G = 1.3 \times 10^7 Pa, \nu = 0$, $k = 1.0 \times 10^{-13}(m^3 s/kg)$;
Consolidation coefficient	$c = (2Gk^*/\gamma) = 2.6 \times 10^{-6}(m^2/s)$;
Time factor	$\tau = (ct/a^2) = 0.1$ where $t = 38\,500s$;
Running properties	$a = 1m, dt = 3850s, \theta = 1$ # steps $= 10$;
2-D mesh properties	linear triangles (1455 nodes, 2736 elements);
Boundary 1	$\sigma_t = 0, \sigma_n = p_o, p = 0$;
Boundary 2	$u_n = 0, \sigma_t = 0, (\partial p/\partial n) = 0$;
Boundary 3	$\sigma_t = 0, \sigma_n = 0, p = 0$;
Boundary 4	$\boldsymbol{u} = 0, (\partial p/\partial n) = 0$;
Boundary 5	$\sigma_t = 0, \sigma_n = 0, p = 0$;
Initial conditions	at $t = 0, \boldsymbol{u} = 0$, and $p = 0$.

The solution is compared to the analytical result reported by Schiffman *et al.* [38] in Fig. 5 for the pore pressure distribution when the position $(x/a) = 0$. With respect to the pore pressure, the result in Fig. 5 showed no error greater than 1.9% of applied load.

In previous work [32], Basser used consolidation theory to create a model of infusion-induced swelling in the brain as two concentric spheres where the internal sphere served as the infusion core. Fig. 6 is a finite element representation of the typical geometry described by Basser. Following the same solution procedure, we considered the following problem as our third benchmark.

Material properties	$G = 6.0 \times 10^3\ Pa, \nu = 0.4891$, $k = 5.0 \times 10^{-12}$(m^{3}s/kg);

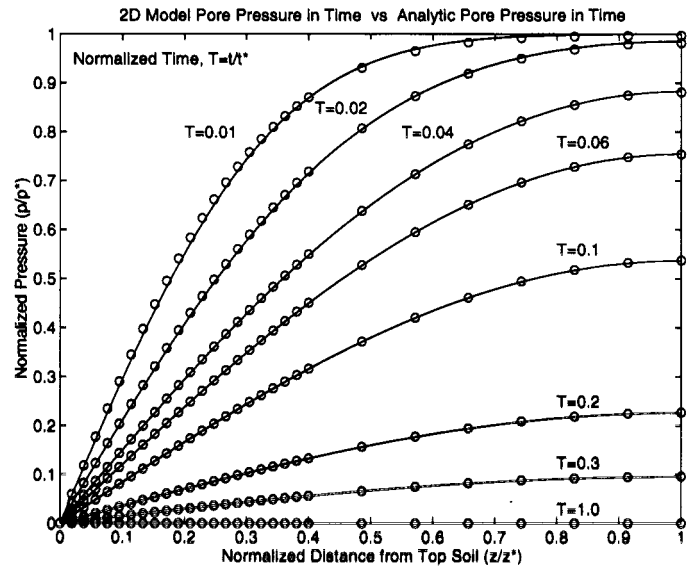

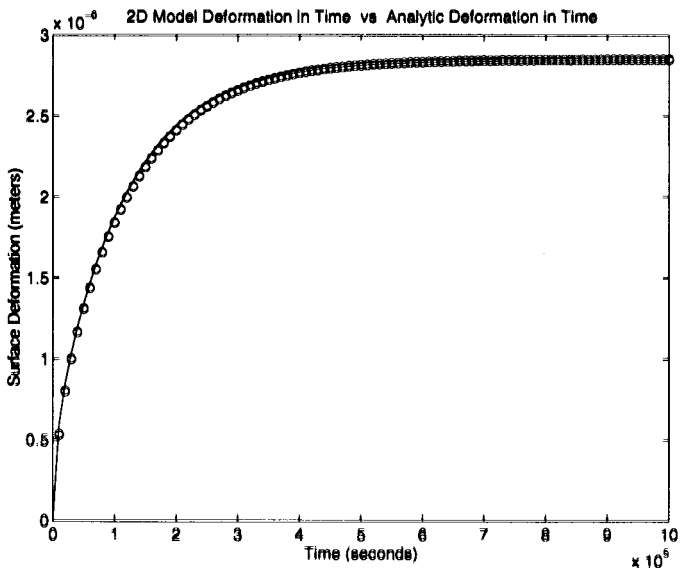

Fig. 2. Two-dimensional plane strain consolidation comparison normalized for $z^* = 1$ m, $p^* = p_o$ (o numerical, — analytical).

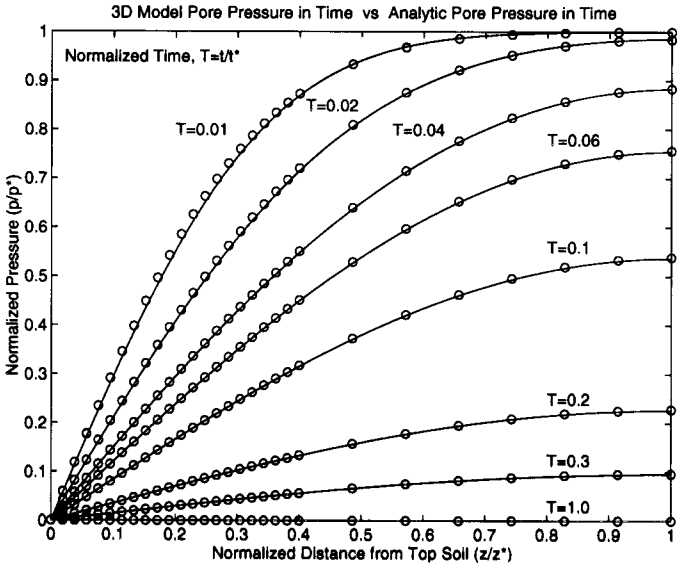

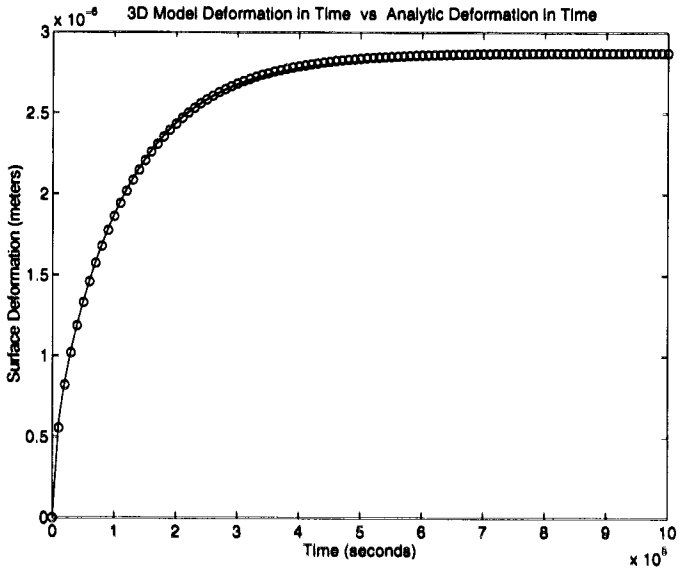

Fig. 3. Three-dimensional consolidation comparison normalized for $z^* = 1$ m, $p^* = p_o$ (o numerical, — analytical).

Running properties	$a = 3.0 \times 10^{-4}\ m, dt = 100\ s,$ $\theta = 1,$ # steps $= 20;$
3-D mesh properties	linear tetrahedral (11227 nodes, 63 411 elements);
Surface 1	$\sigma_n = 0, \sigma_s = 0, \sigma_t = 0, p = p_o;$
Surface 2	$\boldsymbol{u} = 0, p = 0;$
Initial conditions	at $t = 0, \boldsymbol{u} = 0,$ and $p = 0.$

where σ_s and σ_t are the two orthogonal components of shear stress on the 3-D surface. In Fig. 7, the analytic and calculated values at steady state are in excellent agreement and the error is 0.4% of applied load and 2.8% of maximum displacement for pressure and deformation, respectively. Following this comparison, we also solved the problem a second time replacing the Surface 2 boundary condition with

Surface 2	$\sigma_n = 0, u_s = 0, u_t = 0, p = 0;$
Running Properties	$dt = 5.0 \times 10^{-3} s,$ # steps $= 20.$

where u_s and u_t are the displacements tangential to the 3-D surface. Similar to the 2-D striploading case, a finite geometry is utilized and solutions are compared in Fig. 8 during the early transient period in order to avoid influences from the finite boundaries. Assessment of the transient solution accuracy in Fig. 8 shows that the maximum error is no more than 2.2% of the applied load.

V. Animal Model Studies

In this section we report our initial experience with the computational model in predicting deformation in pig brain tissue. These studies require the placement of small nonperturbing CT or MRI-visible markers in brain tissue; these markers can be monitored for motion resulting from manipulations

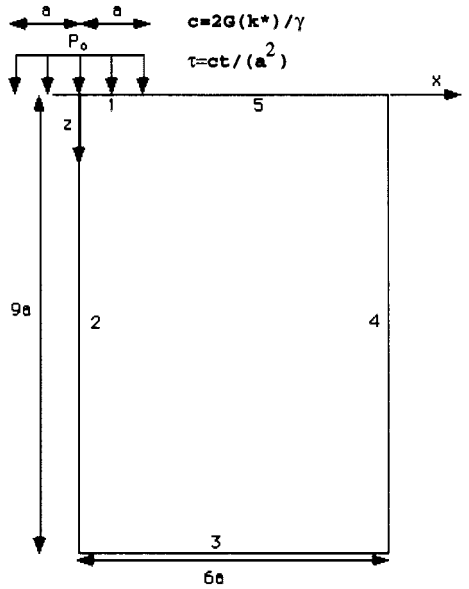

Fig. 4. Two-dimensional striploading benchmark problem ($a = 1$ m).

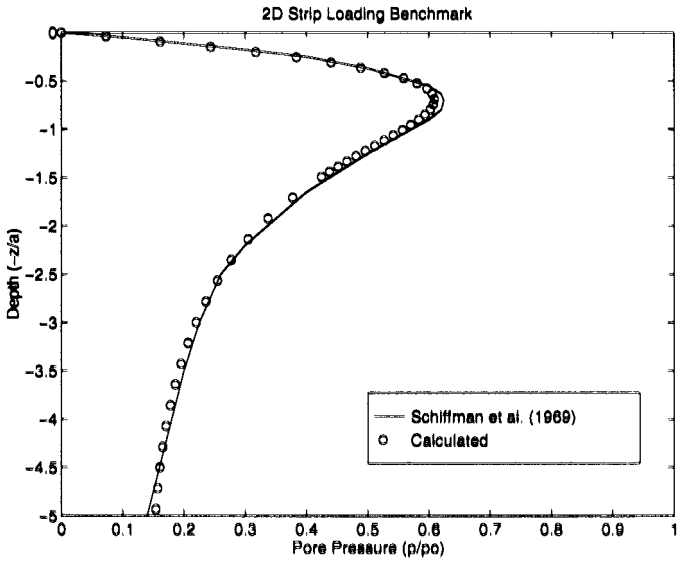

Fig. 5. Two-dimensional striploading benchmark results.

representative of surgical loads. Our purpose here is not to report on the details of our experimental animal protocols for marker placement but rather to provide an overview of the experimental techniques which have been utilized and to establish the preliminary performance of the model in actual tissue.

Fig. 9 shows an example from an *ex-vivo* pig brain with a single centrally located marker which has been displaced by inflating a balloon catheter. In this case the marker is fusinite, which is an inert maceral of coal (component of coal derived from woody plant tissue) that can be prepared to a predetermined particle size by selective grinding and filtering [39]. Subsequent to craniotomy a small amount (0.1 ml) of fusinite material was injected into the pig brain. Fig. 9(a) is a coronal MR image taken after fusinite injection and placement of a deflated balloon catheter, laterally between the parietal

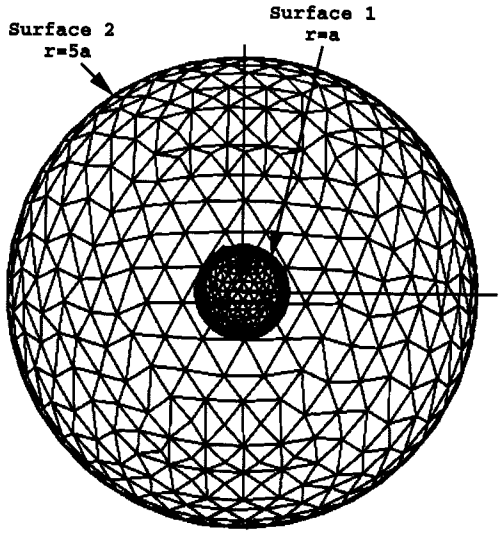

Fig. 6. Three-dimensional sphere benchmark problem ($a = 3.0 \times 10^{-4}$ m).

cranium and cortical surface. The presence of the fusinite can be readily seen (as a local dark spot within the image) and its location has been demarked by the circular cursor shown in the image. To induce a deformation, the balloon was inflated with 2-cc of contrast agent and another image in exactly the same plane was immediately recorded as shown in Fig. 9(b). With the original circular cursor location as a reference, the inflation of the balloon is readily evident and the shift of the fusinite is clear. Using the image analysis software available on the MRI system, we determined that the fusinite was shifted by 4.6 mm medially ($\Delta_x = 4.43$ mm, $\Delta_y = -1.27$ mm).

We have also simulated this experiment with a 2-D version of the finite element model described earlier without the fluid pressure component since the brain tissue is *ex-vivo*. A finite element mesh was constructed based on the anatomy of Fig. 9(a) where the location of the fusinite marker was captured from the preprocedure (balloon deflated) image and represented by a single node in the finite element mesh. Tissue property values for gray and white matter (Young's modulus of 8×10^3 Nm^{-2}, and 4×10^3 Nm^{-2} for gray and white matter, respectively, and Poisson's ratio of 0.47 for both tissue types) were taken from Takizawa *et al.* [29] and displacement boundary conditions determined from the inflated balloon [Figure 9(b)] were applied. The computational results are displayed in Fig. 10(a)–(b), which is the model counterpart to the experimental images shown in Fig. 9(a)–(b). The node corresponding to the fusinite marker was predicted to move 4.6 mm ($\Delta_x = 4.46$ mm, $\Delta_y = -1.16$ mm) which is in remarkable agreement with the experimental results and suggests that the computational model holds some promise in the present application.

We have extended this initial experimental modeling experience to the case of an *in-vivo* pig brain where a much more extensive marker implant has been used and the full 3-D displacement fields have been measured experimentally and computed numerically. In these experiments, prior to any implantation, a high-resolution set of MR images are obtained and serve as the basis for finite element discretization. We

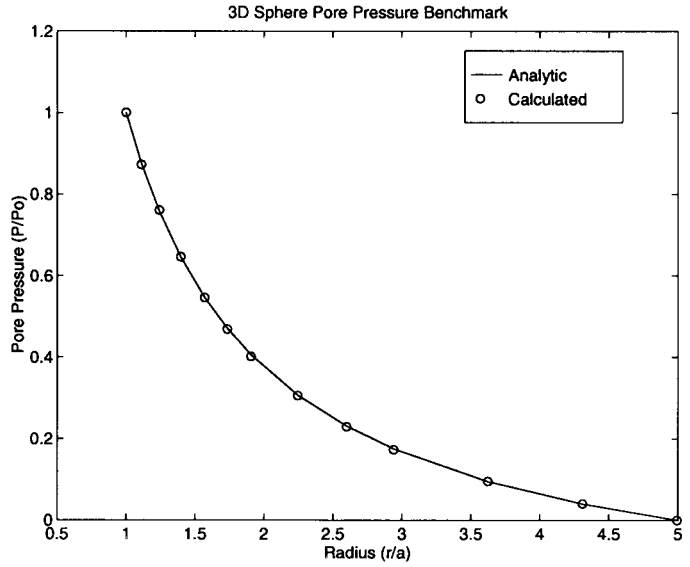

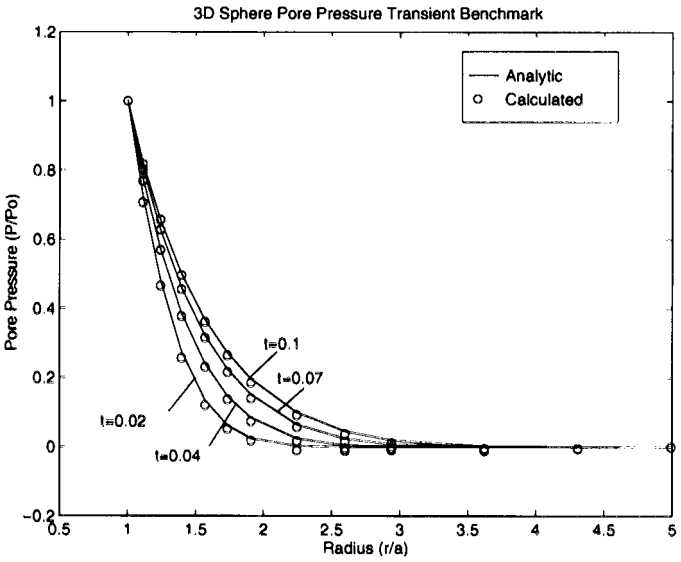

Fig. 8. Three-dimensional transient sphere benchmark problem.

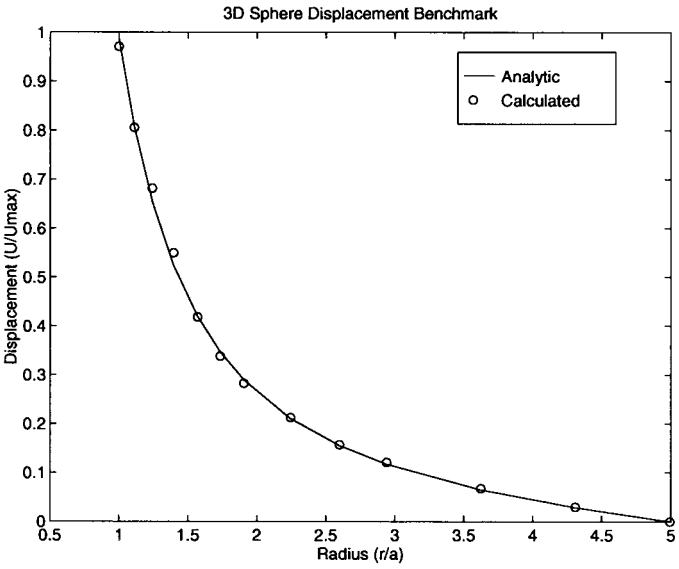

Fig. 7. Three-dimensional sphere consolidation benchmark comparison.

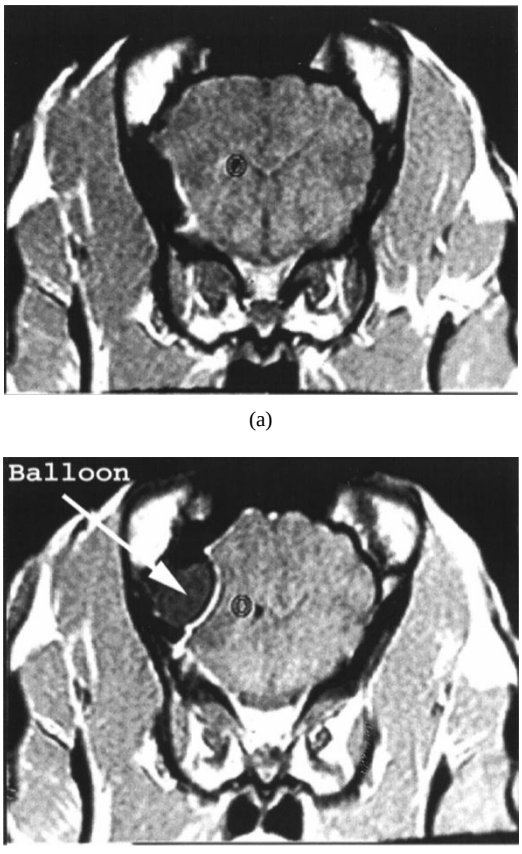

(a)

(b)

Fig. 9. MRI of an *ex vivo* pig brain with a centrally located fusinite marker and balloon catheter placed laterally between the cranium and cortical surface: (a) uninflated balloon with circular cursor centered on the fusinite location; (b) inflated balloon resulting in a medial shift of the fusinite. Cursor remains positioned in the original fusinite location.

use ANALYZE Version 7.5-Biomedical Imaging Resource[1] to segment the volume of interest and MATLAB to render a surface boundary description from which we produce a tetrahedral grid based on the mesh generation algorithms developed by Sullivan *et al.* [40]. Fig. 11(a) displays a typical mesh where volume elements representing the tissue away from the catheter are approximately 1 mm^3 in size whereas those near the implanted (uninflated) balloon catheter have volumes of 0.025 mm^3. Fig. 11(b) contains a computed result after 1-cc balloon inflation as described below. The meshes shown in Fig. 11 contain 11 923 nodes and 62 439 elements.

During the surgical procedure, the pig brain is implanted with small 1 mm diameter beads which are inserted directly into the parenchyma in a grid-like fashion and serve as tracking markers. During this procedure, a portable fluoroscope is used to evaluate marker fixation in the tissue. If markers are found to move subsequent to their initial placement, they are eliminated from the study as tissue movement indicators. In the experiment reported here, an array of 16 markers on a 0.75 cm spacing was used with 14 beads proving to be stationary

[1] ANALYZE software was provided in collaboration with the Mayo Foundation, Rochester, MN.

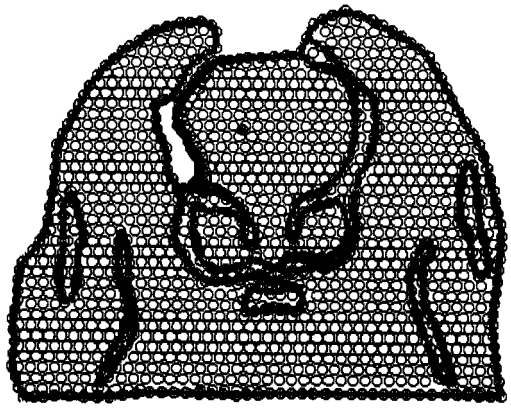

(a)

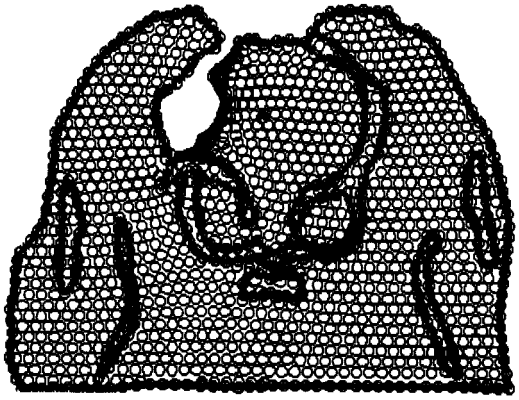

(b)

Fig. 10. FEM model of the balloon inflation experiment shown in Fig. 9(a), (b): (a) model of Fig. 9(a) showing the uninflated balloon with the fusinite location indicated by the darkened node; (b) simulation of Fig. 9(b) showing predicted movement of the fusinite marker (darkened node) resulting from balloon inflation. Experimental and computational agreement is within 0.1 mm.

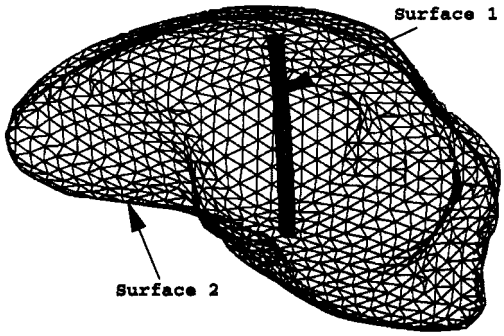

(a)

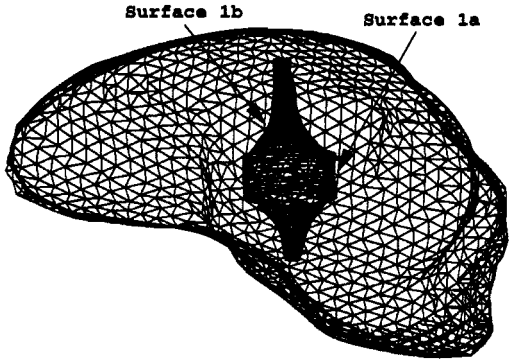

(b)

Fig. 11. Three-dimensional volume meshes (a) preinflation computational model with balloon catheter (b) deformed computational model after simulated 1-cc inflation of balloon catheter.

once placed in the tissue. Following marker implantation, the balloon catheter, filled with contrast agent, is also inserted into the cranium. In this particular case a central balloon insertion was used but placements similar to that shown in Fig. 9(a) have also been used. All implants are readily observed in CT images and are monitored during balloon inflations which are intended to mimic surgical loads. Coregistration of the preoperative MRI with the during-procedure CT is performed to utilize the high-definition MRI information on the pig brain anatomy. At the current stage of model development this step is not essential, as the gray/white matter boundaries have not been incorporated into the FE mesh (i.e., the current model is a homogenous mass with no internal brain structures being resolved).

Fig. 12(a), (c), (e) shows volume representation of the CT data preinflation and during inflation where the parenchymal tissue has been thresholded out in order to display the marker beads and balloon catheter. Quantitative measures of the bead displacements represented as changes in Cartesian coordinates are given in Table I. This experiment has also been modeled using the following parameters.

Material properties $E = 2100\ Pa, \nu = 0.45,$
$k = 1.0 \times 10^{-7}\ (m^3 s/kg);$

Running properties $dt = 1.0 \times 10^4\ s,$
$\theta = 1,$
steps $= 5.$

It should be noted that these material parameters are well within the range of physiological limits, especially given the fact that there is very little consistent data on *in vivo* brain material properties [32], [24], [25].

In terms of boundary conditions, the balloon catheter [Surface 1 in Fig. 11(a)] was divided into two sections which included deformed [Surface 1a in Fig. 11(b)] and free surface components [Surface 1b in Fig. 11(b)]. The deforming surface consisted of boundary conditions which specified the displacement associated with the expanding balloon front [assumed to be uniform in the normal direction, see Fig. 11(b)] while the free surface portion of the catheter was allowed to move freely but assumed not to undergo any normally directed stress. The interstitial pressure at the balloon/tissue interface was taken to be constant at 6000 Pa (or 45 mmHg) which is within the range of values recorded by Wolfla *et al.* [41], [42] under conditions of acute balloon inflation within a closed cranial cavity of the pig. The outer cortical brain surface [Surface 2 in Fig. 11(a)] was prescribed as a fixed (no displacement) boundary with zero fluid pressure. These conditions are summarized as follows.

Surface 1a $u_n = -5.45 \times 10^{-3}$ m,
$\sigma_s = 0, \sigma_t = 0,\ p = 6000$ pa
$= 45$ mmHg;

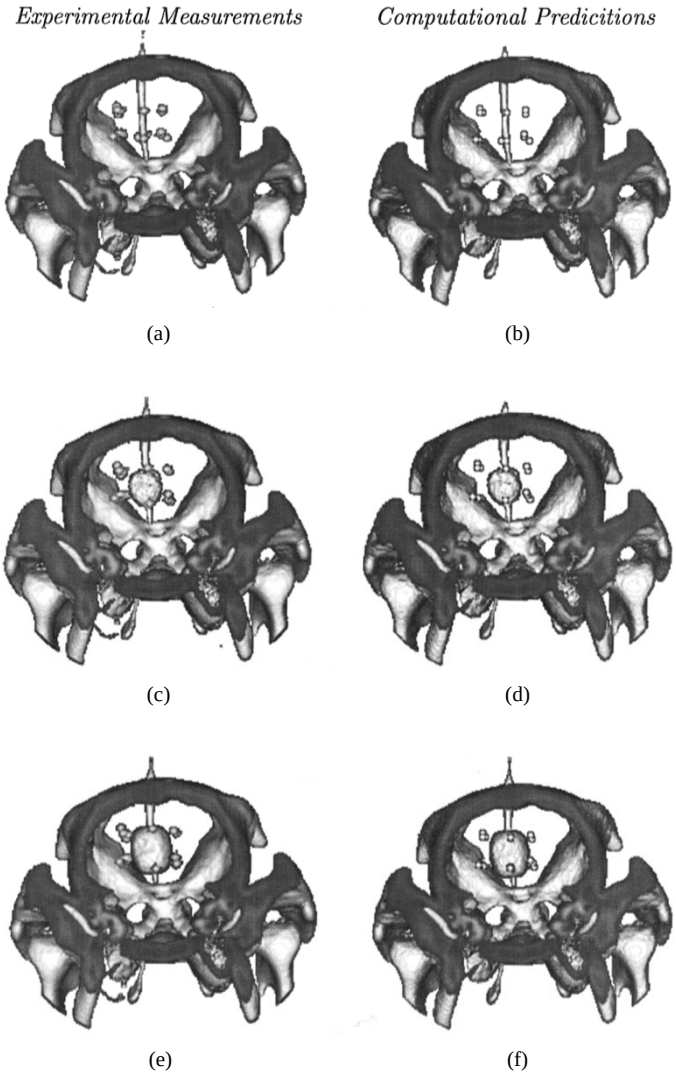

Fig. 12. Experimental porcine model with centrally placed balloon catheter, tissue thresholded out, and surrounding grid of 1-mm stainless steel markers with experimentally and computationally determined positions, respectively: (a) and (b) baseline volume with uniflated catheter; (c)–(d) 1-cc inflation with subsequent bead movement; (e) and (f) 2-cc inflation with subsequent bead movement.

TABLE I
MEASURED BEAD DISPLACEMENT FOR 1-CC AND 2-CC INFLATIONS OF THE BALLOON CATHETER

Bead	1cc inflation (mm)				2cc inflation (mm)			
#	dx	dy	dz	D	dx	dy	dz	D
1	0.00	0.47	-0.47	0.66	-0.47	0.94	-0.47	1.15
2	-0.47	0.00	0.00	0.47	-0.94	0.00	0.00	0.94
3	-0.47	0.00	0.00	0.47	-0.47	0.47	0.47	0.81
4	-0.47	0.00	0.00	0.47	-0.47	0.47	0.00	0.66
5	-0.47	0.00	-0.94	1.05	-0.94	0.00	-0.94	1.32
6	-0.94	-0.47	1.40	1.75	-1.40	-0.47	2.34	2.77
7	0.47	0.00	-0.94	1.05	0.47	0.47	-1.40	1.55
8	0.94	-0.47	0.94	1.40	0.94	-0.47	1.40	1.75
9	0.00	-0.47	-0.47	0.66	-0.47	-0.47	-0.47	0.81
10	-0.94	-1.40	0.94	1.93	-1.87	-1.87	1.40	3.00
11	-0.47	-0.94	1.40	1.75	-0.47	-1.40	1.87	2.39
12	0.47	-0.47	0.00	0.66	0.00	-0.47	-0.47	0.66
13	0.94	-0.47	0.00	1.05	1.87	-0.94	0.00	2.09
14	0.00	0.00	0.47	0.47	0.47	0.00	0.94	1.05

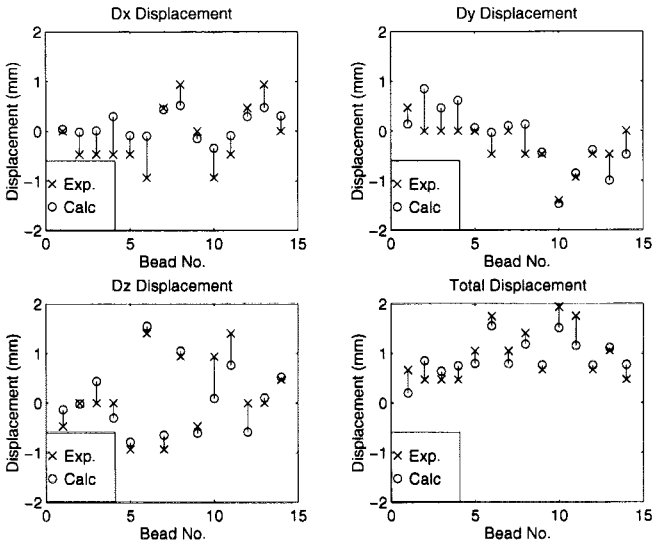

Fig. 13. Comparison between measured and calculated data for directional and total displacements for 1-cc inflation of balloon catheter.

TABLE II
CALCULATED BEAD DISPLACEMENT FOR 1-CC AND 2-CC INFLATIONS OF THE BALLOON CATHETER

Bead	1cc inflation (mm)				2cc inflation (mm)			
#	dx	dy	dz	D	dx	dy	dz	D
1	0.04	0.14	-0.13	0.20	0.04	0.15	-0.14	0.21
2	-0.02	0.85	-0.02	0.85	-0.03	0.90	-0.02	0.91
3	0.01	0.46	0.44	0.64	0.01	0.49	0.46	0.67
4	0.30	0.62	-0.30	0.75	0.32	0.63	-0.31	0.78
5	-0.09	0.07	-0.79	0.79	-0.10	0.07	-0.84	0.85
6	-0.10	-0.03	1.55	1.55	-0.12	-0.03	1.69	1.69
7	0.44	0.10	-0.65	0.79	0.46	0.10	-0.67	0.82
8	0.52	0.14	1.05	1.18	0.55	0.14	1.11	1.25
9	-0.15	-0.43	-0.61	0.76	-0.16	-0.46	-0.64	0.81
10	-0.34	-1.47	0.09	1.51	-0.37	-1.58	0.09	1.62
11	-0.09	-0.86	0.76	1.15	-0.09	-0.91	0.81	1.23
12	0.29	-0.38	-0.58	0.76	0.31	-0.40	-0.61	0.79
13	0.47	-1.00	0.10	1.11	0.51	-1.06	0.11	1.18
14	0.31	-0.47	0.52	0.77	0.32	-0.49	0.54	0.80

Surface 1b	$\sigma_n = 0, \sigma_s = 0, \sigma_t = 0, (\partial p/\partial n) = 0;$
Surface 2	$\boldsymbol{u} = 0, p = 0;$
Initial conditions	at $t = 0$, $\boldsymbol{u} = 0$, and $p = 0$.

The deformed computational geometry for the 1-cc inflation is illustrated in Fig. 11(b). The computed displacement information for each bead is provided in Table II and projected onto the brain anatomy in Fig. 12(b), (d), (f). Fig. 13 quantitatively illustrates the difference between the measured and calculated bead movement for the 1-cc inflation level in each Cartesian direction as well as the total magnitude of displacement. The mean directional error for the computed bead displacements are 0.38, 0.33, and 0.28 mm in the x, y, and z directions with an overall average displacement magnitude error of 0.29 mm. While the general trends in bead displacement have been correctly captured with some bead motions being predicted quite accurately, the quantitative assessments indicate that the model generally underpredicts the actual displacements that have been measured experimentally. Examining Table II reveals that the same conclusion can be drawn about the 2-cc inflation as well.

There are a number of factors which may be contributing to the underprediction and further study is needed to evaluate the potential sources of data/model mismatch. For example, the present mesh does not discriminate gray and white matter which have significantly different elastic properties. Typically gray matter is considered stiffer than white matter with a Young's modulus varying from 2–10 times greater in magnitude than white matter [24], [27]. Property heterogeneity is readily incorporated into the computational model (in fact, the finite element formulation and implementation presented here allows for property heterogeneity) but requires a technique for segmenting the relevant tissue types in the MR images and relating these regions to corresponding elements in the finite element mesh. An automated voxel-by-voxel method for including property heterogeneity directly from the MR scans into the finite element model has recently been described and is under evaluation [43].

In addition, the pressure gradient within the brain over the time scale of the acute inflations which have been performed is largely unknown but acts as a distributed body force that will increase overall deformation. Wolfla *et al.* [41], [42] have shown that large pressure transients in the porcine brain exist under temporally and frontally located balloon catheter placements. We have begun to measure pressure during the inflation procedures and find similar trends [15] but have yet to map spatial distributions which are critical for the model. Another source of error is the applied boundary conditions, where we have approximated the balloon inflation as a combination of a normal displacement with a free floating boundary. By matching more exactly the expanding balloon front, better results can be expected. Variations in both elastic properties and pressure gradient distributions can also be used to improve the data/model match. For example, in the particular experimental results evaluated here, property variations of 5% in Young's modulus and Poisson's ratio improve the data/model match by approximately 0.5, 5%, respectively. These parameter alterations would appear to be within the physiologically reasonable range given the current uncertainties in the actual values for these parameters.

Other factors include the concentrated fluid space within the sulci and gyri of the cortical surface, which have not been explicitly modeled. These may manifest as effective property changes within the model, which could explain why property changes improve the data/model match. Significant nonlinearities, both geometric and material, could also be at play which ultimately limit the validity of the small strain linearly elastic model development we have pursued here. Again, the finite element method is well-suited to incorporating these types of model complexities. The extent to which nonlinearities need to be explicitly included in the model awaits further investigation. Nonetheless, we are encouraged by the degree with which the computations emulate the 3-D *in vivo* motion especially when considering the fact that the model is in a very early stage of development.

VI. Clinical Implications

It is interesting to speculate on how a model-guided technique for updating the registration of preoperative images during the course of neurosurgery might be deployed clinically. We envision that the method would require multiple inputs obtained concurrently with surgery using low cost, readily available instrumentation. For example, brain surface tracking devices could be used to extract boundary condition data for the model. Further, intraoperative ultrasound could be employed to follow a limited amount of subsurface structure (e.g., ventricle surfaces) which would be incorporated into the model in the form of internal motion constraints. Readily available sensors could be used during a surgical procedure to monitor interstitial pressures and applied tissue retractor forces, thereby becoming data input streams for the model as well. The preoperative MR images would also be available for constructing a patient-specific anatomical mesh at the outset of a case to which model-guided deformations would be applied. If tissue heterogeneity turns out to be an important component in the model and is found to vary on a patient-by-patient basis, this preoperative information on individual patient anatomy will become even more important. Further, techniques for deriving tissue parameters preoperatively such as MR elastography and diffusion imaging will need to be developed for this application.

Clearly, to impact clinical decision-making in the OR would require on-line computations which are sufficiently accurate and robust. While the anatomical models reported herein consumed several hours of computation time on a high-end workstation, calculations on the order of 5–10 min are not inconceivable in the near future and still potentially useful, clinically. In fact, we have not considered the optimization of our algorithms to date. Further, a number of the time-consuming computational tasks could be precomputed prior to the surgery. For example, matrix assemblies and preconditioners could be computed in advance in which case only time-stepping would need to be performed in the OR. Even in our present codes, a time-step can be executed in less than 10 min on our current mesh discretizations. In terms of accuracy, Roberts *et al.* have recently reported that the cortical surface moves as much as 1 cm on average during typical surgeries [8]. Other studies have emerged which suggest similar degrees of motion [44], [45]. Hence, if a model-guided approach were able to recapture 50%–75% of this motion, that is, be accurate to within a few millimeters, it would likely be an improvement over maintaining preoperative image registration throughout an entire surgery.

Validating a model-guided approach *in vivo* using animal model systems appears to be readily feasible and we are currently pursuing this course. Phantom models can be used to demonstrate the valid integration of surface and subsurface data acquisition using OR tools with model calculations. However, obtaining complete validation of the model-guided approach in human subjects is considerably more complex and constrained. This will likely have to occur in a setting where intraoperative CT/MR scanning is available for comparing volumetric brain motion with model estimates. Fortunately, the model-guided approach is not likely to fail catastrophically because it will be constrained by physical data obtained in the OR. Further, the preoperative image database would always be available to the neurosurgeon; hence, doubts about

the reliability of the model-updated image space can be considered from the perspective of the preoperative image space coupled with previous clinical experience. Even if the technique is not perfectly accurate, it may well be able to recover some portion of the misregistration error which occurs during surgery without itself introducing significant new misalignments.

Beyond on-line computations for correcting misregistration errors during surgery, development of this model offers potential uses as a preplanning and/or educational tool to assist neurosurgeons in understanding the potential ramifications of tissue motion for a particular procedural approach. Modeling of neuropathophysiologies, for example, the development and resolution of hydrocephalus, is another area of interest where simulation could be beneficial [24]–[28], although there is considerable work to be done in developing meaningful relationships between the observed physical responses to be modeled and the underlying physiological processes that drive a particular condition. Establishing the utility of our computational scheme in any of these applications will require extensive model validation studies. In the model-updated frameless stereotactic neurosurgical context, we have begun this work in a porcine brain system and hope to report on our findings in the near future.

VII. Conclusions

We have formulated, implemented and begun *in vivo* testing of a 3-D finite element model of brain tissue deformation under comparable surgical loads. The computational scheme is based on a linearly elastic porous media physical model which has been adapted from the soil mechanics literature. Benchmark cases for both 2-D and 3-D calculations have been considered and the computational results clearly show that the mathematical framework has been solved with high fidelity. Errors with known solutions or published computations are less than 3% for both displacement and pressure variables.

Initial simulations of experiments conducted in actual brain tissue of a pig model are also encouraging. *Ex vivo* studies are particularly satisfying and submillimetric accuracy in predicted displacement for a single marker has been observed. In this case the fluid pressure component is essentially nonexistent, leaving only the elastic response of the solid tissue to be considered. Agreement between computed and measured *in vivo* results are not as dramatic at this stage, although clearly the correct trends in a complete 3-D array of markers displaced under acute balloon catheter inflation have been predicted with the model. In this case, the overall mean displacement error is approximately 14% for the 1-cc balloon inflation and 19% for the 2-cc balloon inflation, which suggests that the magnitude of displacement is being approximated reasonably correctly. Given that the model at this point is linear, homogenous with simple boundary conditions, these results are extremely encouraging.

One major unknown in the existing model is the pressure gradient distribution that develops under acute balloon inflation. Simulations which vary this parameter by approximately 40% translate into improvements of 5% in model performance. Whether such distributions do indeed exist in practice awaits further study. Hence, it appears that combinations of property variation and pressure gradient distribution development may be able to account for a significant portion of the data/model mismatch which exists under baseline conditions. Given the current uncertainty in these parameters, the overall model performance is viewed as encouraging, although it must be acknowledged that nonlinearities in the response of brain tissue to surgical loads may also be important factors which may ultimately need to be incorporated into the computational model.

Appendix

The discrete form represented in (7b)–(7d) does not materialize directly from the discrete version of (6) but requires some further manipulation of its boundary and volume terms. Specifically, the boundary integral terms in (6a) can be rearranged to produce the normal stress boundary integrals in (7d) provided that some additional alterations in volume integrations are also made. For example, in 2-D Cartesian coordinates the x-component of the boundary integrals in (6a) becomes

$$\hat{x}\cdot\left[\oint G\hat{n}\cdot\nabla\boldsymbol{u}\phi_i\,ds+\oint\frac{G}{1-2\nu}\hat{n}(\nabla\cdot\boldsymbol{u})\phi_i\,ds\right]=\oint\left[\frac{2G(1-\nu)}{1-2\nu}n_x\frac{\partial u_x}{\partial x}+Gn_y\frac{\partial u_x}{\partial y}+\frac{G}{1-2\nu}n_x\frac{\partial u_y}{\partial y}\right]\phi_i\,ds \tag{8a}$$

whereas the corresponding x-component boundary integral in (7d) can be expressed as

$$\hat{x}\cdot\oint\sigma_s\cdot\hat{n}\phi_i\,ds=\oint\left[\frac{2G(1-\nu)}{1-2\nu}n_x\frac{\partial u_x}{\partial x}+Gn_y\frac{\partial u_x}{\partial y}\right]\phi_i\,ds+\oint\left[\frac{2G\nu}{1-2\nu}n_x\frac{\partial u_y}{\partial y}+Gn_y\frac{\partial u_y}{\partial x}\right]\phi_i\,ds \tag{8b}$$

which leaves $\oint(G/1-2\nu)n_x(\partial u_y/\partial y)\phi_i\,ds$ from (8a) compared to $\oint[(2G\nu/1-2\nu)n_x(\partial u_y/\partial y)+Gn_y(\partial u_y/\partial x)]\phi_i\,ds$ from (8b) as terms which do not balance. Now, it can be readily shown that

$$\begin{aligned}\left\langle G\frac{\partial u_y}{\partial y}\ \frac{\partial\phi_i}{\partial x}\right\rangle&=\left\langle G\frac{\partial}{\partial x}\left(\frac{\partial u_y}{\partial y}\phi_i\right)\right\rangle-\left\langle G\frac{\partial}{\partial y}\left(\frac{\partial u_y}{\partial x}\phi_i\right)\right\rangle+\left\langle G\frac{\partial u_y}{\partial x}\ \frac{\partial\phi_i}{\partial y}\right\rangle\\&=\oint G\left[n_x\frac{\partial u_y}{\partial y}-n_y\frac{\partial u_y}{\partial x}\right]\phi_i\,ds+\left\langle G\frac{\partial u_y}{\partial x}\ \frac{\partial\phi_i}{\partial y}\right\rangle\end{aligned} \tag{9}$$

is the only domain integration that would exist in the x-component of (6a) whose discrete form does not directly appear in (7). However, replacing this term with the right-hand-side of (9) yields a discretized domain integration which does appear in (7) (e.g., $G\delta_{xy}$ in the first row, second column of A_{ij} in (7b) instead of $G\delta_{yx}$) plus boundary integrals that

can be combined with the unaccountable term in (8a) to form

$$\oint \left[\frac{G}{1-2\nu} n_x \frac{\partial u_y}{\partial y} + G n_y \frac{\partial u_y}{\partial x} - G n_x \frac{\partial u_y}{\partial y} \right] \phi_i \, ds = \oint \left[\frac{2G\nu}{1-2\nu} n_x \frac{\partial u_y}{\partial y} + G n_y \frac{\partial u_y}{\partial x} \right] \phi_i \, ds \tag{10}$$

which is identical to the unaccounted boundary terms in (8b). Thus, the 3-D Cartesian coordinate equivalent of the relationship

$$\begin{aligned} \hat{x} \cdot \left[\oint G \hat{n} \cdot \nabla \boldsymbol{u} \phi_i \, ds + \oint \frac{G}{1-2\nu} \hat{n} (\nabla \cdot \boldsymbol{u}) \phi_i \, ds \right] \\ + \oint G \left[n_x \frac{\partial u_y}{\partial y} - n_y \frac{\partial u_y}{\partial x} \right] \phi_i \, ds \\ = \hat{x} \cdot \oint \sigma_s \cdot \hat{n} \phi_i \, ds + \left\langle G \frac{\partial u_y}{\partial y} \; \frac{\partial \phi_i}{\partial x} \right\rangle \\ - \left\langle G \frac{\partial u_y}{\partial x} \; \frac{\partial \phi_i}{\partial y} \right\rangle \end{aligned} \tag{11}$$

allows the natural boundary integrals in (6a) to be reexpressed as the normal stress components and discrete domain integration modifications shown in (7).

REFERENCES

[1] T. Peters, B. Davey, P. Munger, R. Comeau, A. Evans, and A. Olivier, "Three-dimensional multimodal image-guidance for neurosurgery," *IEEE Trans. Med. Imag.*, vol. 15, pp. 121–128, 1996.

[2] W. E. L. Grimson, G. J. Ettlinger, S. J. White, T. Lozano-Perez, W. M. Wells, III, and R. Kikinis, "An automated registration method for frameless stereotaxy, image guided surgery and enhanced reality visualization," *IEEE Trans. Med. Imag.*, vol. 15, pp. 129–140, 1996.

[3] D. W. Roberts, J. W. Strohbehn, J. F. Hatch, W. Murray, and H. Kettenberger, "A frameless stereotactic integration of computerized tomographic imaging and the operating microscope," *J. Neurosurg.*, vol. 65, pp. 545–549, 1986.

[4] R. L. Galloway, R. J. Maciunas, and C. A. Edwards, "Interactive image-guided neurosurgery," *IEEE Trans. Biomed. Eng.*, vol. 39, pp. 1226–1231, 1992.

[5] G. H. Barnette, D. W. Kormos, and C. P. Steiner, "Use of a frameless, armless stereotactic wand for brain tumor localization with 2-D and 3-D neuroimaging," *Neurosurg.*, vol. 33, pp. 674–678, 1993.

[6] D. R. Sanderman and S. S. Gill, "The impact of interactive image guided surgery: the Bristol experience with the ISF/Elekta viewing wand," *Acta Neurochirurgica, Suppl.*, vol. 64, pp. 54–58, 1995.

[7] K. R. Smith, K. J. Frank, and R. D. Bucholz, "The NeuroStation—A highly accurate, minimally invasive solution to frameless stereotactic neurosurgery," *Comput. Med. Imag. Graph.*, vol. 18, pp. 247–256, 1994.

[8] D. W. Roberts, A. Hartov, F. E. Kennedy, M. I. Miga, and K. D. Paulsen, "Intraoperative brain shift and deformation: A quantitative clinical analysis of cortical displacements in 28 cases," *Neurosurg.*, vol. 43, pp. 749–758, 1997.

[9] H. Erbe, A. Kriete, A. Jodicke, W. Deinsberger, and D. K. Boker, "3-D Ultrasonography and image matching for detection of brain shift during intracranial surgery," *Comput. Assist. Radiol.*, Hulemke *et al.* Ed., 1996, pp. 225–230.

[10] L. D. Lunsford, "A dedicated CT system for the stereotactic operating room," *Appl. Neurophysiol.*, vol. 45, pp. 374–378, 1982.

[11] J. Koivukangas, Y. Louhisalmi, and J. Alakuijala *et al.*, "Ultrasound controlled neuronavigator-guided brain surgery," *J. Neurosurg.*, vol. 79, pp. 36–42, 1993.

[12] P. D. Leroux, T. C. Winter, M. S. Berger, L. A. Mack, K. Wang, and J. P. Elliott, "A comparison between preoperative magnetic resonance and intraoperative ultrasound tumor volumes and margins," *J. Clin. Ultrasound*, vol. 22, pp. 29–36, 1994.

[13] T. M. Moriarty, R. Kikinis, F. A. Jolesz, P. M. Black, and E. Alexander, III, "Magnetic resonance imaging therapy. Intraoperative MR imaging.," *Neurosurg. Clin. N. Amer.*, vol. 7, pp. 323–331, 1996.

[14] M. Biot, "General theory of three dimensional consolidation," *J. Appl. Phys.*, vol. 12, pp. 155–164, 1941.

[15] M. I. Miga, K. D. Paulsen, F. E. Kennedy, P. J. Hoopes, A. Hartov, and D. W. Roberts, "A 3-D brain deformation model experiencing comparable surgical loads," in *Proc. Annu. Int. Conf. IEEE Eng. Med. Biol. Soc.*, Chicago, IL, 1997, pp. 773–776.

[16] T. A. Shugar and M. G. Katona, "Development of a finite element head injury model," *ASCE J. Eng. Mech. Div.*, vol. EM3, no. E101/173, pp. 223–239, 1975.

[17] C. C. Ward and R. B. Thompson, "The development of a detailed finite element brain model," in *Proc. 19th Stapp Car Crash Conf.*, 1975, pp. 641–674.

[18] T. B. Khalil and R. P. Hubbard, "Parametric study of head response by finite element modeling," *J. Biomech.*, vol. 10, pp. 119–132, 1977.

[19] J. A. Ruan, T. B. Khalil, and A. I. King, "Human head dynamic response to side impact by finite element modeling," *ASME J. Biomech. Eng.*, vol. 113, pp. 276–283, 1991.

[20] C. Ljung, "A model for brain deformation due to rotation of the skull," *J. Biomech.*, vol. 8, pp. 263–274, 1975.

[21] E. K. Walsh, W. Furniss, and A. Schettini, "On measurement of brain elastic response *in vivo*," *Amer. J. Physiol.*, vol. 232, pp. R27–R30, 1977.

[22] E. K. Walsh and A. Schettini, "Calculation of brain elastic parameters *in vivo*," *Amer. J. Physiol.*, vol. 247, pp. R693–R700, 1984.

[23] G. T. Fallenstein, and V. D. Huke, "Dynamic mechanical properties of brain tissue," *J. Biomech.*, vol. 2, pp. 217–226, 1969.

[24] T. Nagashima, T. Shirakuni, and SI. Rapoport, "A two-dimensional, finite element analysis of vasogenic brain edema," *Neurol. Med. Chir.*, vol. 30, pp. 1–9, 1990.

[25] T. Nagashima, Y. Tada, S. Hamano, M. Skakakura, K. Masaoka, N. Tamaki, and S. Matsumoto, "The finite element analysis of brain oedema associated with intracranial meningiomas," *Acta. Neurochir. Suppl.*, vol. 51, pp. 155–157, 1990.

[26] T. Nagashima, N. Tamaki, M. Takada, and Y. Tada, "Formation and resolution of brain edema associated with brain tumors. A comprehensive theoretical model and clinical analysis," *Acta Neurochir. Suppl.*, vol. 60, pp. 165–167, 1994.

[27] Y. Tada and T. Nagashima, "Modeling and simulation of brain lesions by the finite-element method," *IEEE Eng. Med. Biol., Mag.*, 1994, pp. 497–503.

[28] H. Takizawa, K. Sugiura, M. Baba, C. Kudou, S. Endo, M. Nakabayashi, and R. Fukuya, "Deformation of brain and stress distribution caused by putaminal hemorrhage—numerical computer simulation by finite element method," *No To Shinkei*, vol. 43, pp. 1035–1039, 1991.

[29] H. Takizawa, K. Sugiura, M. Baba, and J. D. Miller, "Analysis of intracerebral hematoma shapes by numerical computer simulation using the finite element method," *Neurol. Med. Chir.*, vol. 34, pp. 65–69, 1994.

[30] D. G. Taylor, J. L. Bert, and B. D. Bowen, "A mathematical model of interstitial transport. I. Theory," *Microvasc. Res.*, vol. 39, pp. 253–278, 1990.

[31] ———, "A mathematical model of interstitial transport. II. Microvasculature exchange in the mesentery," *Microvasc. Res.*, vol. 39, pp. 279–306, 1990.

[32] P. J. Basser, "Interstitial pressure, volume, and flow during infusion into brain tissue," *Microvasc. Res.*, vol. 44, pp. 143–165, 1992.

[33] K. K. Mendis, R. L. Stalnaker, and S. H. Advani, "A constitutive relationship for large deformation finite element modeling of brain tissue," *J. Biomech. Eng.*, vol. 117, pp. 279–285, 1995.

[34] R. L. Spilker and J. K. Suh. "Formulation and evaluation of a finite element model for the biphasic model of hydrated soft tissue," *Comp. Struct.*, vol. 35, no. 4, pp. 425–439, 1990.

[35] R. L. Spilker and T. A. Maxian. "A mixed-penalty finite element formulation of the linear biphasic theory for soft tissues," *Int. J. Numer. Meth. Eng.*, vol. 30, pp. 1063–1082, 1990.

[36] J. P. Laible, D. Pflaster, B. R. Simon, M. H. Krag, M. Pope, and L. D. Haugh, "A dynamic material parameter estimation procedure for soft tissue using a poroelastic finite element model," *J. Biomech. Eng.*, vol. 116, pp. 19–29, 1994.

[37] C. T. Hwang, N. R. Morgenstern, and D. W. Murray, "On solutions of plane strain consolidation problems by finite element methods," *Can. Geotech. J.*, vol. 8, pp. 109–118, 1971.

[38] R. L. Schiffman, A. T-F. Chen, and J. C. Jordan. "An analysis of consolidation theories," *J. Soil Mech., Foundations Division, Proc. ASCE*, pp. 285–312, 1969.

[39] N. Vahidi, R. B. Clarkson, K. J. Liu, S. W. Norby, M. Wu, and H. M. Swartz, "*In vivo* and *in vitro* EPR oximetry with fusinite: A new coal derived, particulate EPR probe," *Magn. Reson. Med.*, vol. 31, pp. 139–146, 1994.

[40] J. M. Sullivan Jr., G. Charron, and K. D. Paulsen, "A three dimensional mesh generator for arbitrary multiple material domains," *Finite Element Anal., Design*, vol. 25, pp. 219–241, 1997.

[41] C. E. Wolfla, T. G. Luerssen, R. M. Bowman, and T. K. Putty, "Brain tissue pressure gradients created by expanding frontal epidural mass lesion," *J. Neurosurg.*, vol. 84, pp. 642–647, 1996.
[42] C. E. Wolfla, T. G. Luerssen, and R. M. Bowman, "Regional brain tissue pressure gradients created by expanding extradural temporal mass legion," *J. Neurosurg*, vol. 86, pp. 505–510, 1997.
[43] M. I. Miga, K. D. Paulsen, F. E. Kennedy, P. J. Hoopes, A. Hartov, and D. W. Roberts, "Initial *in-vivo* analysis of 3-D heterogeneous brain computations for model-updated image-guided neurosurgery," in *"Medical Image Computing and Computer-Assisted Intervention—MICCAI '98,"* W. M. Wells, A. Colchester, and S. Depl, Eds. in *Lecture Notes in Computer Science*, vol. 1496. Berlin, Germany: Springer-Verlag, 1998, pp. 743–752.
[44] D. L. G. Hill, C. R. Maurer, M. Y. Wang, R. J. Maciunas, J. A. Barwise, and J. M. Fitzpatrick, "Estimation of intraoperative brain surface movement," in *Proc. CVRMed-MRCAS'97*; J. Troccaz, E. Grimson, and R. Mosges, Eds., Springer Lecture Notes in Computer Science, vol. 1205, pp. 449–458, 1997.
[45] H. Dickhaus, K. Ganser, A. Staubert, M. M. Bonsanto, C. R. Wirtz, V. M. Tronnier, and S. Kunze, "Quantification of brain shift effects by mr-imaging," *Proc. Annu. Int. Conf. IEEE Eng. Med. Biol. Soc.*, 1997, pp. 491–494.

Keith D. Paulsen (S'85–M'86) received the B.S. degree in biomedical engineering from Duke University, Durham, NC, in 1981 and the M.S. and Ph.D. degrees in biomedical engineering from Dartmouth College, Hanover, NH, in 1984 and 1986, respectively.

From 1986 to 1988, he was an Assistant Professor in the Electromagnetics Group within the Department of Electrical and Computer Engineering, University of Arizona, Tucson. He is currently an Associate Professor at the Thayer School of Engineering, Dartmouth College and the Director of the Radiobiology and Bioengineering Research Program for the Norris Cotton Cancer Center within the Dartmouth-Hitchcock Medical Center, Lebanon, NH. His research interests include computational methods with particular emphasis on biomedical problems in cancer therapy and imaging, and model-guided surgery.

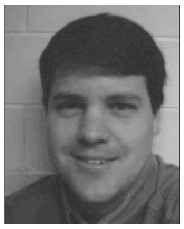

Michael I. Miga was born in 1969. He was educated at the University of Rhode Island, Kingston, RI (URI) and received the B.S. degree in mechancical engineering in 1992. He continued at URI to receive the M.S. degree (also in mechanical engineering) in 1994, specializing in the design of controllers using convex optimization techniques. He is currently pursuing the Ph.D. degree at Dartmouth College's Thayer School of Engineering, Hanover, NH, developing a 3-D brain deformation model for model-updated image-guided neurosurgery.

In the latter half of his tenure at URI, he worked as a contractor for the Naval Undersea Warfare Center in Newport, RI (1991–1994) on the design of countermeasure launchers for submarines. His research interests include computational modeling in biomedicine and tissue and biofluid mechanics.

He is a 1998 Thayer School Distinguished Fellow.

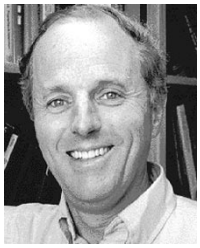

Francis E. Kennedy was educated at received the B.S. degrees from Worcester Polytechnic Institute Worcester, U.K., in 1963 and the M.S. degree from Stanford University, Stanford, CA, in 1965, both in mechanical engineering. He received the Ph.D. degree in mechanics from Rensselaer Polytechnic Institute Troy, NY, in 1973.

Since 1974, he has been on the faculty of Thayer School of Engineering at Dartmouth College, Hanover, NH, where he is now Professor of Engineering. His research activity has been in the following areas: biomechanics, tribology, experimental and numerical methods in contact mechanics, biomechanics, and heat transfer. He is the author or co-author of over 80 technical papers and four book chapters and has edited four books (symposium volumes). He is Chief Technical Editor of the *ASME Journal of Tribology* (1993–1998).

Dr. Kennedy is a Fellow of STLE and ASME.

P. Jack Hoopes was born in Muskogee, OK, in 1951. He was an undergraduate student at the University of Oklahoma, Norman, OK, (1969–1972). He received the DVM degree from the College of Veterinary Medicine, Oklahoma State University, Stillwater, in 1976. He completed residencies in; exotic animal medicine and pathology, National Zoologiocal Park, Smithsonian Institution, Washington DC (1977–1979) and Pathology, College of Veterinary Medicine, Colorado State University, Ft Collins (1979–1982). He completed the Ph.D degree in pathology and radiation biology, Colorado State University in 1984. Following graduation he completed postodoctoral fellowships in veterinary oncology at the Comparative Oncology Unit, Colorado State University (1985) and the North Carolina Animal Cancer Treatment Program, College of Veterinary Medicine, North Carolina State University and the Department of Radiation Oncology, Duke University, Durham, NC (1986–1987).

In 1988, he became an Assistant Professor of Medicine (Radiation Oncology) and Surgery (Neurosurgery), Dartmouth Medical School, He is currently an Associate Professor or Medicine and Surgery, Director of the Surgery and Radiation Research Laboratories and an Adjunct Associate Professor of Bioengineering at the Thayer School of Engineering, Dartmouth College. His research interests include the pathobiology of radiation-tissue interactions and the use of radiation, hyperthermia, and photodynamic therapy (PDT) and immunology to treat cancer.

Alex Hartov was born in France in August 1957. He received the BSEE degree with High Honors from Northeastern University, Boston, MA, in 1984. He received the M.S. degree in medical imaging and 3-D reconstruction in 1988 and the Ph.D. degree in intraoperative ultrasound hyperthermia in 1991, both from the Thayer School of Engineering, Hanover, NH.

He spent six years as Electronics Design Engineer while in school and after. He is currently Research Assistant Professor at the Dartmouth Medical School and the Thayer School of Engineering. Current projects and interests in: brain deformation, electrical impedance spectroscopy, microwave imaging, coronary artery stress distribution, and prostate hyperthermia. He is a part time consultant in biomedical related projects.

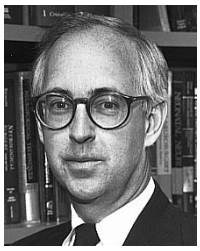

David W. Roberts received the A.B. degree from Princeton University, Princeton, NJ, the M.A. degree from Oxford University, Oxford, U.K., and the M.D. degree from Dartmouth Medical School, Hanover, NH.

He is Professor of Surgery (Neurosurgery) at Dartmouth Medical School and Chairman of Neurosurgery at the Dartmouth-Hithcock Medical Center. His research interests are in the areas of frameless stereotaxy and intractable epilepsy.

Dr. Roberts is President of the American Society of Stereotactic and Functional Neurosurgery.